






An Upper Limit on the Mass of a Central Black Hole in the Large Magellanic Cloud from the Stellar Rotation Field

H. Boyce^{1,2} , N. Lützgendorf², R. P. van der Marel^{2,3} , H. Baumgardt⁴, M. Kissler-Patig⁵,
N. Neumayer⁶ , and P. T. de Zeeuw^{7,8}

¹ Department of Physics and McGill Space Institute, McGill University, 3600 University Street, Montreal QC, H3A 2T8, Canada; boyceh@physics.mcgill.ca

² Space Telescope Science Institute, 3700 San Martin Drive, Baltimore, MD 21218, USA

³ Center for Astrophysical Sciences, Department of Physics & Astronomy, Johns Hopkins University, Baltimore, MD 21218, USA

⁴ School of Mathematics and Physics, The University of Queensland, St. Lucia, QLD 4072, Australia

⁵ Gemini Observatory, Northern Operations Center, 670 N. A'ohoku Place, Hilo, HI 96720, USA

⁶ Max-Planck-Institut für Astronomie, Königsstuhl 17, D-69117 Heidelberg, Germany

⁷ European Southern Observatory (ESO), Karl-Schwarzschild-Strasse 2, D-85748 Garching, Germany

⁸ Sterrewacht Leiden, Leiden University, Postbus 9513, 2300 RA Leiden, The Netherlands

Received 2016 November 27; revised 2017 July 24; accepted 2017 July 28; published 2017 August 28

Abstract

We constrain the possible presence of a central black hole (BH) in the center of the Large Magellanic Cloud. This requires spectroscopic measurements over an area of the order of a square degree, due to the poorly known position of the kinematic center. Such measurements are now possible with the impressive field of view of the Multi Unit Spectroscopic Explorer (MUSE) on the ESO Very Large Telescope. We used the Calcium Triplet (~ 850 nm) spectral lines in many short-exposure MUSE pointings to create a two-dimensional integrated-light line-of-sight velocity map from the $\sim 10^8$ individual spectra, taking care to identify and remove Galactic foreground populations. The data reveal a clear velocity gradient at an unprecedented spatial resolution of 1 arcmin^2 . We fit kinematic models to arrive at a 3σ upper-mass limit of $10^{7.1} M_\odot$ for any central BH—consistent with the known scaling relations for supermassive black holes and their host systems. This adds to the growing body of knowledge on the presence of BHs in low-mass and dwarf galaxies, and their scaling relations with host-galaxy properties, which can shed light on theories of BH growth and host system interaction.

Key words: black hole physics – galaxies: individual (Large Magellanic Cloud) – galaxies: kinematics and dynamics

1. Introduction

As one of our closest neighbors, the study of the Large Magellanic Cloud (LMC) provides insights into many branches of astrophysics. These topics include studies of stellar populations (e.g., Nikolaev & Weinberg 2000; Van der Swaelmen et al. 2013), the interstellar medium (e.g., Dickey & Lockman 1990; Schenck et al. 2016), microlensing by dark objects (e.g., Alcock et al. 2000), and the cosmological distance scale (e.g., Walker 2012). In addition, many recent photometric and kinematic data sets have shown that the inner regions of the LMC are dynamically complex (e.g., Zhao & Evans 2000; Olsen & Salyk 2002). An understanding of the structure and kinematics of the LMC is necessary for all of these applications. As a potential host of an intermediate-mass black hole (IMBH) or a supermassive black hole (SMBH) at its center, the LMC can also help constrain models of early universe BH seed formation as well as the scaling relations of BHs and their host systems in the lower-mass range. Here we present a new study of the stellar kinematics near the center of the LMC, and use this to provide the first constraints on the possible presence of a central BH.

Over the years, the relations between BH mass and properties of their host galaxies such as bulge stellar velocity dispersion, bulge luminosity, and bulge mass have been extensively studied (Ferrarese & Merritt 2000; Gebhardt et al. 2000; Marconi & Hunt 2003; Häring & Rix 2004; Gültekin et al. 2009; Kormendy & Ho 2013; McConnell & Ma 2013). While these relations suggest a co-evolution between galaxies and their BHs, they remain poorly constrained for both

lower-mass BHs ($M_{\text{BH}} \lesssim 10^6 M_\odot$) and lower-mass host systems ($M_* \lesssim 10^{10} M_\odot$).

In the last 10–15 years, detections of active galactic nuclei (AGNs) in nearby dwarf galaxies have provided a means of filling in the lower-mass range of the BH mass/host galaxy property relations (e.g., Filippenko & Ho 2003; Barth et al. 2004; Reines et al. 2011; Baldassare et al. 2015; den Brok et al. 2015). Lately, more systematic surveys have been done by sampling larger data sets (e.g., Greene & Ho 2007; Reines et al. 2013). However, the measurements for BHs in dwarf galaxies are still relatively scarce, often have high uncertainties, and none are near enough to study using detailed kinematics of their stars.

SMBH ($\geq 10^6 M_\odot$) are found in the centers of virtually all massive galaxies (e.g., Kormendy & Ho 2013). The most distant SMBHs are seen as quasars with redshifts indicating that they existed at a time when the universe was less than a billion years old (e.g., Mortlock et al. 2011). It is still not understood how BHs could become this massive on such a short timescale. In contrast to very massive galaxies, the fraction of dwarf galaxies with massive BHs at their centers is currently unknown. The non-detection of a massive BH in M33 (Gebhardt et al. 2001; Merritt et al. 2001) has shown that the occupation fraction for low-mass galaxies must be lower than unity. A handful of recent studies have placed constraints of $M_{\text{BH}} \lesssim 10^4\text{--}10^6 M_\odot$ on a few nearby dwarf galaxies (e.g., Filippenko & Ho 2003; Valluri et al. 2005; Barth et al. 2009, 2004; Seth et al. 2010; Reines et al. 2011; Neumayer & Walcher 2012; den Brok et al. 2015). The determination of this fraction for low-mass galaxies ($M_* \lesssim 10^{10} M_\odot$) can help

constrain different theories of the formation of primordial BHs in the first billion years of the universe (Greene 2012).

One explanation for high-redshift BH formation is the existence of “seed” BHs with $M \lesssim 1000 M_{\odot}$ produced by the collapse of Population III stars. This requires super-Eddington accretion to explain the rapid growth of SMBHs in the early universe (e.g., Madau et al. 2014). If this mechanism is the primary source of seed BHs in the early universe, it predicts that nearly all ($>90\%$) present-day low-mass ($M_{*} \sim 10^9 M_{\odot}$) galaxies necessarily contain BHs at their centers (Greene 2012). On the other hand, another theory proposes the existence of more massive seed BHs of masses on the order of $\sim 10^{4-5} M_{\odot}$ produced from the direct collapse of pre-galactic disks and gas clouds in the early universe (e.g., Begelman et al. 2006; Lodato & Natarajan 2006). This theory predicts that $\sim 50\%$ of present-day dwarf galaxies would contain central BHs (Greene 2012). Depending on the mechanism for these primordial BHs’ formation, Volonteri & Natarajan (2009) found that the slope and scatter in the $M_{\text{BH}}-\sigma$ relation would vary for BH masses $\lesssim 10^6 M_{\odot}$. In either case, it is clear that the search for BHs in the range of $10^{4-6} M_{\odot}$ in dwarf galaxies like the LMC can provide insight into the process of BH formation, growth, and their relationships to their host systems.

Alternatively, there may be signatures of IMBHs in nearby globular clusters (GCs). This can be searched for by measuring the velocity dispersion (σ) of stars near the center. Since GCs around the Milky Way are significantly closer to us relative to almost all other potential hosts of IMBHs, the “sphere-of-influence” of any BH becomes a larger angle on the sky, and therefore possible to probe through stellar motions. The existence of IMBHs in nearby GCs remains a topic of ongoing discussion. To date, there has been no evidence of accretion of IMBH’s in the centers of GCs through X-ray or radio observations (Maccarone et al. 2005; Strader et al. 2012). Some kinematic evidence for the presence of IMBHs ($10^{4-5} M_{\odot}$) in GCs has been found from studies with Integral Field Units (IFUs; e.g., Noyola et al. 2008; Lützgendorf et al. 2011; Feldmeier et al. 2013). However, these claims have been challenged by groups measuring the velocity dispersion with proper motions (Anderson & van der Marel 2010; McNamara et al. 2012) and measurements of individual radial velocities (Lanzoni et al. 2013).

Spectroscopic techniques for constraining the presence of BHs in galaxy centers using stellar or gaseous kinematics are well established, and typically use a slit or small IFU field placed at the galaxy center. However, application of these techniques to the LMC poses the unique challenge that the exact position of its center is poorly determined. There are two reasons for this. First, since the LMC is relatively close to us (~ 50 kpc away), it spans an enormous area on the sky. Stars can be traced to $\sim 10^{\circ}$ and beyond on either side (e.g., Besla et al. 2016). Second, the morphology of the LMC (the prototype of the class of Magellanic *Irregular* galaxies) is asymmetric. The photometric center differs from the kinematic center by more than a degree (e.g., Kallivayalil et al. 2013; van der Marel & Kallivayalil 2014; see Figure 1). Also, its kinematics are complex, disturbed, and poorly understood. These features are due to its ongoing interaction with the Small Magellanic Cloud and Milky Way (Hatzidimitriou et al. 1993; Cole et al. 2005; Besla et al. 2012).

Hence, despite many existing studies of the LMC, the position of its kinematic center is only known to ~ 30 arcmin.

The best available constraints come from the analysis of the velocity fields of HI gas (Luks & Rohlfs 1992; Kim et al. 1998) and stellar proper motions (van der Marel & Kallivayalil 2014). So to constrain the possible presence of a central BH, it is necessary to spectroscopically map an area of about a square degree. This is well beyond the capabilities of almost all existing spectrographs, given reasonable amounts of exposure time. However, the most powerful IFU ever built, the Multi Unit Spectroscopic Explorer (MUSE) instrument, was recently commissioned on the ESO Very Large Telescope (VLT). In this paper, we report the results of using MUSE to map the largest region in the LMC ever measured spectroscopically in integrated light, using many pointings with short-exposure times over a square degree area surrounding the kinematic center (see Figure 1). Through this method, we combine the velocities of many individual stars to build up a velocity field and determine the rotation curve, and use these to search for the kinematic signature of a BH.

Section 2 of the paper details these observations and the data reduction, while Section 3 describes the construction of the velocity map and subsequent comparison to BH models. Using this line-of-sight (LOS) velocity map and the derived rotation curve, we set an upper-mass limit on any BH within the central degree of the LMC. We put the results into the context of dwarf galaxies and their BHs in Section 4.

2. MUSE Observations and Data Reduction

Our observations were collected with MUSE on the VLT of ESOs La Silla Paranal Observatory in Chile under the program 094.B-0566. MUSE is a second generation instrument designed for the VLT (Bacon et al. 2010). It includes an IFU that operates toward the red in the visual wavelength range (465–930 nm). We observed in the wide field mode of the instrument, which provided a spatial sampling of $0''.2$ over a field of view that was 1×1 arcmin². This mode captures over 90,000 simultaneous spectra in one pointing, and has a resolving power of 2000 at 465 nm and 4000 at 930 nm. Taking advantage of the excellent spatial coverage provided by this instrument, we observed the central square degree of the LMC with 784 individual pointings separated from one another by 1 arcmin. Therefore, the final data set covers $\sim 25\%$ of the central square degree of the LMC. This is illustrated in Figure 1.

The kinematic centers of the HI and stellar velocity fields and their error bars are contained within this coverage. By running a Monte Carlo simulation of the weighed mean of these two known centers, we are 96.5% certain that the true kinematic center lies within the area covered in our observations. Each pointing contains a 309×317 spaxel image provided by the MUSE IFU. This amounts to spectra of thousands of stars in the central region of interest from which we constructed our velocity map.

Our observations were slated as a filler program on the instrument. Taken on multiple days in November and December of 2014, each pointing had an exposure time of only 60 s allowing us to map a large area of the sky in a short period of time. By later combining the spectra of all the stars in a single pointing, the signal-to-noise ratio (S/N) was built up to form integrated spectra from which accurate velocity measurements could be taken. In this way, each pointing in our observations becomes a data point in the velocity map, representing the average velocity for the LMC stars in that

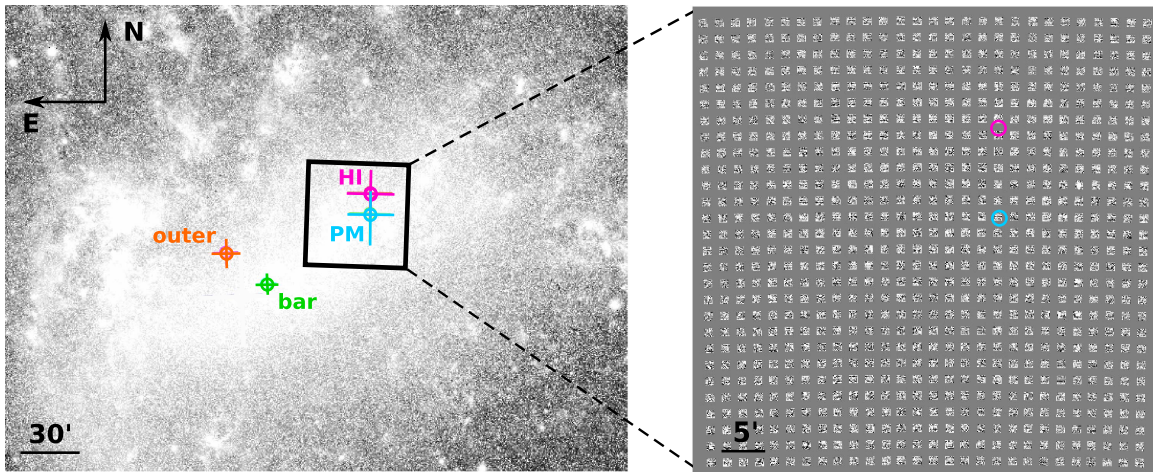


Figure 1. Large Magellanic Cloud with known kinematic and photometric centers. Left panel: central bar of the LMC and its centers determined with different methods. H I: the gas dynamical center of the cold H I disk (Luks & Rohlf 1992; Kim et al. 1998), PM: the stellar dynamical center inferred from a model fit to proper motions by van der Marel & Kallivayalil (2014), bar: the densest point in the bar (de Vaucouleurs & Freeman 1972; van der Marel 2001), outer: the center of the outer isopleths extracted from the 2MASS survey and corrected for viewing perspective by van der Marel (2001). Right panel: the $1^\circ \times 1^\circ$ area observed with MUSE.

field. A representative pointing in S/N units is displayed in Figure 2.

The data reduction was performed with the ESO pipeline designed specifically for MUSE. The preliminary routines (`muse_bias`, `muse_dark`, `muse_flat`, `muse_wavcal`, and `muse_skyflat`) combine calibration frames into master calibrations to be used in the subsequent steps (`muse_sci-basic` and `muse_scipost`), which perform the flat fielding, sky subtraction, and wavelength calibration. A detailed documentation of these routines and their functions can be found in the MUSE Pipeline Manual.⁹

3. Analysis

Within each MUSE pointing, we first identified and excluded foreground sources in the fields before combining all remaining spectra with high enough signal-to-noise into a representative spectrum for that pointing. We then measured a LOS velocity from the Calcium Triplet absorption feature (~ 850 nm) in each spectrum and used this to construct a velocity map. A six-parameter Markov Chain Monte Carlo (MCMC) analysis was used to compare our map to model maps containing a BH of varying masses. The results set a limit on the mass of any BH within the center of the LMC. The following subsections detail these steps.

3.1. Identifying Foreground Sources

To obtain the intrinsic kinematics of the LMC, it was necessary to identify and remove known foreground sources before combining the spectra. To identify all sources within our fields, we used the software Source Extractor (SExtractor; Bertin & Arnouts 1996), which allowed us to create a catalog of stars and their positions in each pointing.

Largely, the default values of the configuration file were used, with the main alterations tabulated in Table 1. `DETECT_MINAREA` is the minimum number of pixels needed to be considered an object. This was increased from a value of five to discourage identifying small, bright image artifacts as stellar sources. Assigning the `FILTER` parameter as

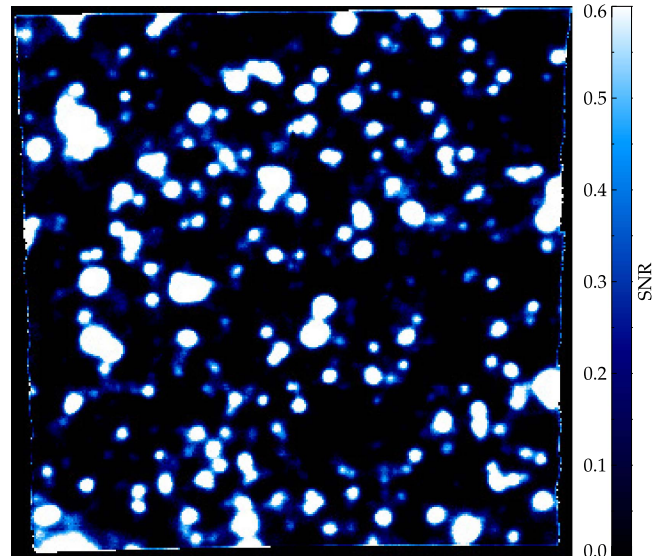


Figure 2. Signal-to-noise map of a typical MUSE field. The area of this field is one arcmin^2 .

Table 1
Altered Parameters in the Source Extractor Configuration File

Parameter	Value
<code>DETECT_MINAREA</code>	30
<code>DETECT_THRESH</code>	1.5
<code>FILTER</code>	<i>N</i>
<code>DEBLEND_MINCONT</code>	0.001

N simply turns the keyword off and prevents a process of smoothing the image before detecting pixels. This was done to prevent sources close together from being smoothed into each other. The smoothing process would be helpful with detecting faint extended objects, and is therefore not useful in our crowded star fields. `DETECT_THRESH` is the detection threshold for determining objects relative to the background root-mean-square (rms) value. Through several trials, a value of 1.5 was determined to best identify the obvious sources in the field. The parameter `DEBLEND_MINCONT` controls the

⁹ Documentation is available at <https://www.eso.org/sci/software/pipelines/muse/>.

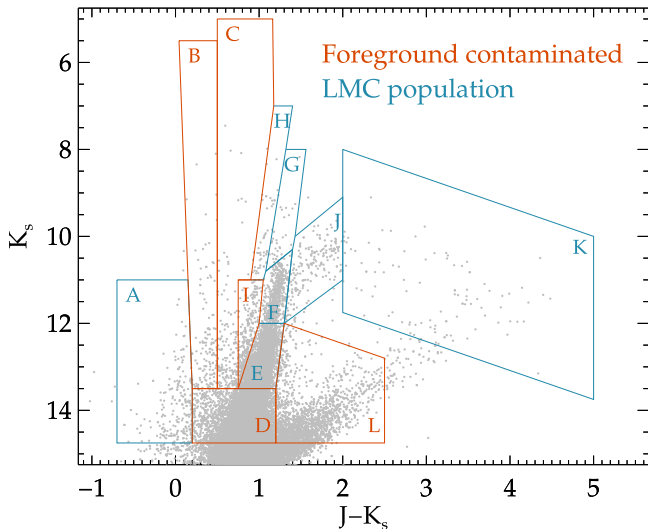


Figure 3. Color–magnitude diagram for LMC sources in both 2MASS and MUSE data overlaid with regions as defined by Nikolaev & Weinberg (2000).

program’s criteria for determining when bright objects close together are separate sources. The value of 0.001 is the fraction that a number of counts in a separate branch of an object has to be above the total count of the object to be flagged as independent. Combining the catalogs into a master list of all positions of sources in the data allowed for easy comparison with the 2MASS catalog—where the foreground sources are known.

Analysis of 2MASS data done by Nikolaev & Weinberg (2000) was used for the identification of foreground stars. The 2MASS survey collected raw imaging data in the near-infrared (NIR) at J ($1.25 \mu\text{m}$), H ($1.65 \mu\text{m}$), and K_s ($2.16 \mu\text{m}$) that covered 99.998% of the celestial sphere between 1997 and 2001 (Skrutskie et al. 2006). The 2MASS All-Sky Point Source Catalog (Skrutskie et al. 2006) provided us with the catalog¹⁰ of all point-source positions and their J , H , and K_s magnitudes within a 3500 arcsec square of the LMC central position R.A. = $5^{\text{h}}16^{\text{m}}57^{\text{s}}$, decl. = $-69^{\text{d}}15^{\text{m}}35^{\text{s}}$. To match our catalog of MUSE sources with the 2MASS source catalog, we used CataXcorr,¹¹ a code specifically developed to perform astrometric matching. This resulted in a complete list of sources in our data for which we had NIR information.

Nikolaev & Weinberg (2000) identified 12 stellar populations from the color–magnitude diagram (CMD; Figure 3 of Nikolaev & Weinberg 2000) constructed from 2MASS data. Shown in Figure 3 is the CMD of the sources identified both in the MUSE data and 2MASS. It is overlaid with the same regions as defined by Nikolaev & Weinberg (2000).

To identify 12 distinct stellar populations, Nikolaev & Weinberg (2000) make use of both the spatial density distribution of 2MASS sources (Figure 4 of Nikolaev & Weinberg 2000) and the theoretical colors/isochrones in the CMD. Through visual inspection of the spatial density distribution of the stars, the regions in the CMD that are heavily foreground contaminated are identified as B, C, D, I, and L, which correspond to the regions of the same

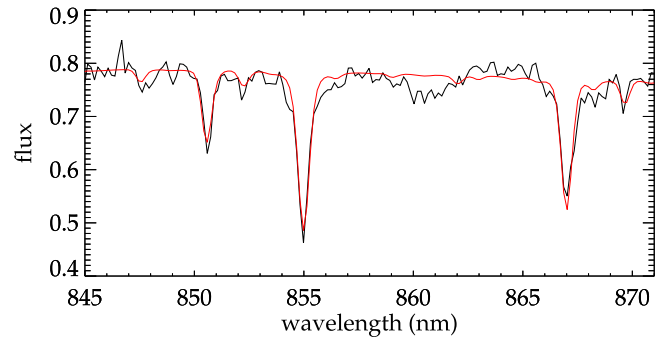


Figure 4. Combined spectrum of a single pointing in the region of the Calcium Triplet. Overplotted in red is the best fit for the spectrum.

classification on the CMD in Figure 3. Any stars identified to fall within these regions of the CMD are flagged within the MUSE data. For a more detailed analysis of these stellar populations, we refer to Nikolaev & Weinberg (2000).

3.2. Extraction of Spectra and Kinematics

To create a velocity map, we constructed representative spectra for each of the 784 pointings in our data set by combining the spaxels we determined to belong to LMC sources. Figure 2 shows a typical S/N map for a MUSE field in the central region of the LMC. S/N maps like the one displayed are used to identify spaxels that had spectra with $S/N > 0.5$ and were therefore considered to belong to sources in the field. Spaxels belonging to foreground sources identified by the analysis of the infrared CMD in Nikolaev & Weinberg (2000) are excluded in all combined spectra. This was achieved by masking out spaxels within a set radius around the spatial location of each foreground source. The spectra were then combined by computing an iteratively sigma-clipped mean on each pixel in the wavelength dimension. To remove the remaining sky signatures not caught in the reduction process, a “sky” spectrum was also generated by combining the $S/N < 0.0$ spaxels. This was then subtracted from the combined signal spectrum to produce the final spectrum of the light from all the LMC stars in the pointing. Each of the 784 spectra representing each MUSE field were made up of an average of 8000 combined spectra within that particular field and had an average S/N of 36.9 in the region of the Calcium Triplet. Figure 4 displays a spectrum representative of the majority of all spectra that were used in measuring radial velocities from the Calcium Triplet absorption lines ($\sim 850 \text{ nm}$).

For each combined spectrum, the penalized pixel-fitting (pPXF) program developed by Cappellari & Emsellem (2004) and Cappellari (2017) was used to determine both LOS velocity and velocity dispersion. Though the spectral resolution of MUSE is not high enough for a meaningful measurement of the internal LMC velocity dispersion (σ), an extreme (too high or too low) value of the velocity dispersion inferred from the fit often indicates some problem with the spectra. When fitting models to our kinematic data, the majority of the fields with velocity measurements that were 3σ away from the best fit also had velocity dispersion measurements greater than 100 km s^{-1} or less than 40 km s^{-1} (approximately the instrumental resolution of MUSE). We therefore found these velocity dispersion criteria to be an acceptable method for rejecting spectra with poor velocity measurements. Additionally, 97% of spectra were fit with an average velocity error of 6 km s^{-1} .

¹⁰ Downloaded from <http://www.ipac.caltech.edu/2mass/releases/allsky/>.

¹¹ Developed by P. Montegriffo at INAF-Osservatorio Astronomico di Bologna. The package is available at <http://davide2.bo.astro.it/~paolo/Main/CataPack.html>.

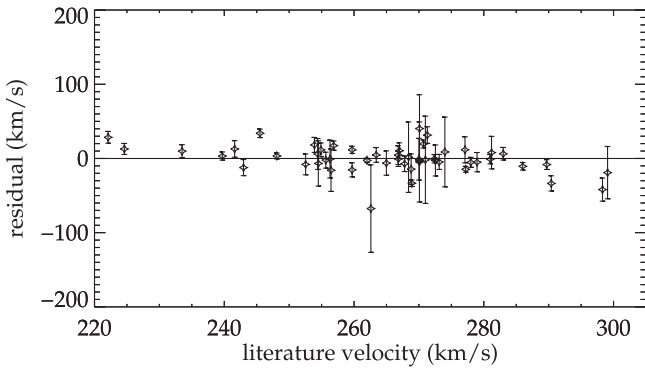


Figure 5. Differences between the known velocity of a star in the literature and the measurement we made from the collected MUSE data plotted against the known literature velocities.

Spectra with velocity errors larger than a 97.5% cut of 26.3 km s^{-1} were also considered unreliable.

The central degree of the LMC contains 256 stellar sources with known radial velocities in the literature, from the compilation of van der Marel & Kallivayalil (2014). Our $\sim 25\%$ coverage of the central degree of the LMC coincides with 69 of these known LOS measurements. As a consistency check, we derived our own velocities for these sources in our MUSE fields using combined spectra of the spaxels belonging to each of these sources and applying the same pPXF method used on the spectra for our velocity map. On average, the signal-to-noise of the spectra for these individual stars was 8.7—much less than that of the combined spectra for the entire MUSE fields (due to the fact that these spectra were constructed from the combination of considerably fewer spaxels). We reject 11 stars that had velocity dispersion measurements above 100 km s^{-1} indicating unreliable velocity measurements, and reject one for having an $S/N < 3$. This left us with 57 acceptable velocity measurements to compare to the known values found in the literature. Figure 5 displays the differences between our velocity measurements of these stars and the known literature values. Error bars come from the uncertainty in the MUSE measurements, where larger error bars correspond to noisier spectra. They are scattered around a weighted mean value of $-0.1 \pm 0.9 \text{ km s}^{-1}$ demonstrating that our measurement of individual stellar velocities have a zero-point in agreement with the literature.

3.3. Modeling

Of the 784 velocity points in our map, we discarded 100 of them on the basis of velocity dispersion measurements above 100 km s^{-1} , below 40 km s^{-1} , or velocity errors above 26 km s^{-1} . These criteria were an indication of an unreliable kinematic measurement—see Section 3.2. This left us with 684 acceptable points to use as constraints for various models. Figure 6 displays our entire 2D velocity field with the rejected points replaced with the best-fit model value at those positions and marked with white crosses. Overplotted with their error bars are the kinematic centers determined in the literature: PM is the stellar kinematic center determined by the *Hubble Space Telescope* (HST) proper motion measurements (van der Marel & Kallivayalil 2014), and HI is the gas dynamical center of the cold HI disk (Luks & Rohlfs 1992; Kim et al. 1998).

To characterize our velocity map, we generate models containing two components: a linear velocity field and the

velocity field due to the gravitational potential of a BH. Since potentials from different mass components add linearly, and since the circular velocity squared at a given radius is proportional to the radial gradient of the gravitational potential, the circular velocity of our model at a given point in the plane of the LMC is given by

$$v_{\text{model}} = \sqrt{v_{\text{linear_lmc}}^2 + v_{\text{BH}}^2}, \quad (1)$$

where the circular velocity of the BH in the inclined LMC plane (v_{BH}) is given by

$$v_{\text{BH}}^2 = GM/r, \quad (2)$$

where M is the mass of the BH in solar masses, G is the gravitational constant in appropriate units, and r is the distance from the BH in degrees (transformed from kpc using the distance to the LMC as 50.1 kpc (Freedman et al. 2001)).

$v_{\text{linear_lmc}}$ in Equation (1) corresponds to the case of solid-body cylindrical rotation, which is a reasonable approximation for the central regions of disk galaxies. This linear component was calculated in the plane of the sky as v_{linear} (see Equation (3)) before being transformed into the LMC plane using an inclination angle 34° (van der Marel & Kallivayalil 2014). This linear component is given by

$$v_{\text{linear}} = v_0 + v_1^*(x' - x_0), \quad (3)$$

where, x' (and y') are coordinates rotated by an angle ϕ up from the horizontal with an origin $(x', y') = (0, 0)$ at (R.A., decl.) = (80.45, -69.70), x_0 is the position of the center about which the plane “pivots,” v_0 is set to the systematic velocity of the LMC ($261.1 \pm 2.2 \text{ km s}^{-1}$ van der Marel & Kallivayalil 2014), and v_1 is the slope of the plane in km s^{-1} per degree. In these coordinates, the position of a modeled BH in the plane of the sky is (x_0, y_0) .

The total model velocity (v_{model}) at each position was then transformed from the LMC plane into the plane of the sky to produce our model velocity maps. Figure 7 shows example models displaying the signatures of $10^6 M_\odot$, $10^7 M_\odot$, and $10^8 M_\odot$ BHs. Clearly, models containing BHs around 10^8 solar masses are strongly ruled out. To be as accurate as possible in the regions near the BH, the fields that vary significantly over a single pointing were divided into subgrids. Any field within 0.2° of the BH position was divided into a subgrid of 50×50 points (avoiding the central singularity), where we evaluated the individual velocity values and then averaged over these to assign a velocity to the entire field. In this way, the model velocity maps in Figure 7 are generated with the same spatial sampling as the map in Figure 6.

To efficiently fit our data to this five-parameter model, we turn to MCMC analysis. We use the EMCEE package developed by Foreman-Mackey et al. (2013), which is an implementation of the affine-invariant MCMC ensemble sampler by Goodman & Weare (2010). This was done by defining a log-likelihood quantity,

$$\begin{aligned} \ln p(v|x_0, v_1, \phi, y_0, \log M_{\text{BH}}) \\ = -\frac{1}{2} \sum_n \left[\frac{(v_{\text{obs},n} - v_{\text{model},n})^2}{s_n^2} + \ln(2\pi s_n^2) \right], \end{aligned} \quad (4)$$

that sums over all valid points in the velocity map. Here, v_{obs} is the measured velocity from the data for that position, v_{model} is

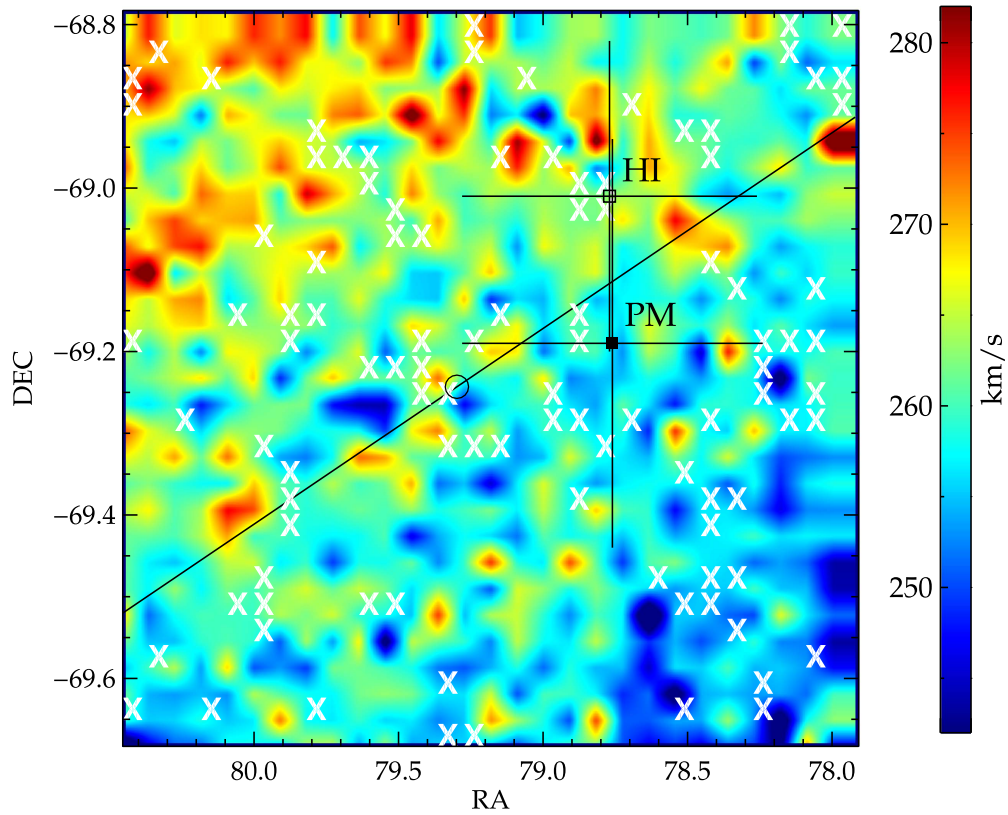


Figure 6. New VLT/MUSE LOS velocity map of the central degree of the LMC. Diagonal line is the central position as fitted by the x_0 parameter in the five-parameter model fit. PM is the kinematic center as determined from proper motion data in van der Marel & Kallivayalil (2014), and H I is the H I gas dynamical center as reported in Luks & Rohlfs (1992) and Kim et al. (1998). White “x”s indicate a field for which a velocity measurement was excluded on the basis of having $\sigma > 100 \text{ km s}^{-1}$, $\sigma < 40 \text{ km s}^{-1}$, $v_{\text{err}} > 26 \text{ km s}^{-1}$, or lying further than 3σ away from the initial model fit. In these locations, the color for the plot was filled in with the velocity value from the best-fit model. The open circle is the location where the model fits a black hole with $\sim 1\sigma$ confidence.

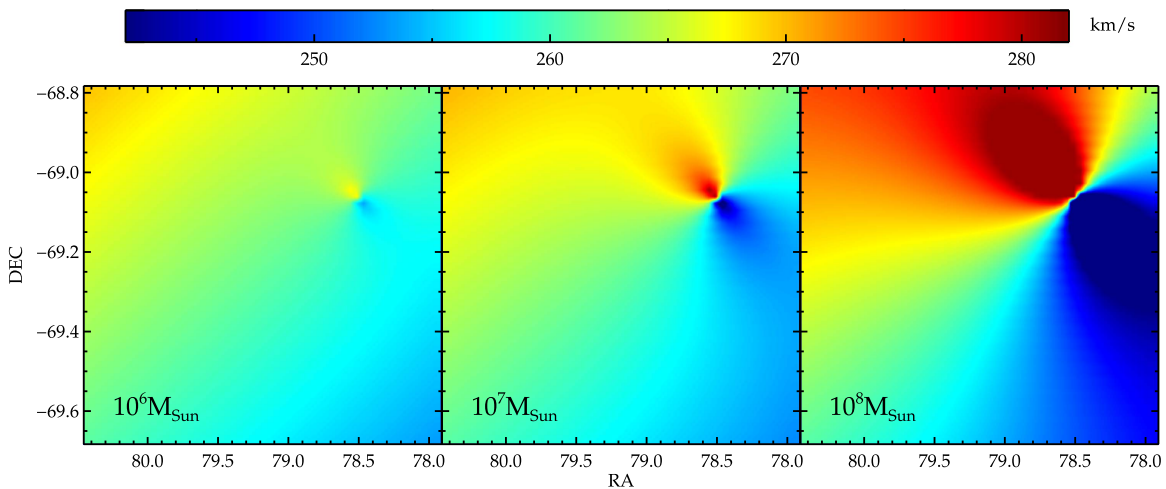


Figure 7. Models of the LMC velocity field with $10^6 M_{\odot}$, $10^7 M_{\odot}$, and $10^8 M_{\odot}$ black holes, over the area surrounding the kinematic center implied by previous measurements. In these plots, the black hole was placed at the kinematic center, but its position was varied in our model fits.

the velocity generated by our model, and s_n^2 is given by

$$s_n^2 = v_{\text{err},n}^2 + f^2 (v_{\text{model},n})^2, \quad (5)$$

where v_{err} is the error obtained by running a Monte Carlo routine with the pPXF software (Cappellari & Emsellem 2004; Cappellari 2017), and f is a sixth parameter of the MCMC that we allowed to vary as the fractional amount our errors could be underestimated by.

After running the MCMC over the 684 points in our map, we rejected an additional field that had a velocity value more than 3σ away from the best-fit model: leaving us with 683 fields. This field was determined to be contaminated by an unusually bright foreground star.

All five parameters of our velocity model plus $\ln f$ are varied in the MCMC and compared with the 683 reliable measurements in the velocity field. Figure 8 shows the result of the MCMC with the best-fit parameters as $x_0 = 0^{\circ}15 \pm 0^{\circ}08$,

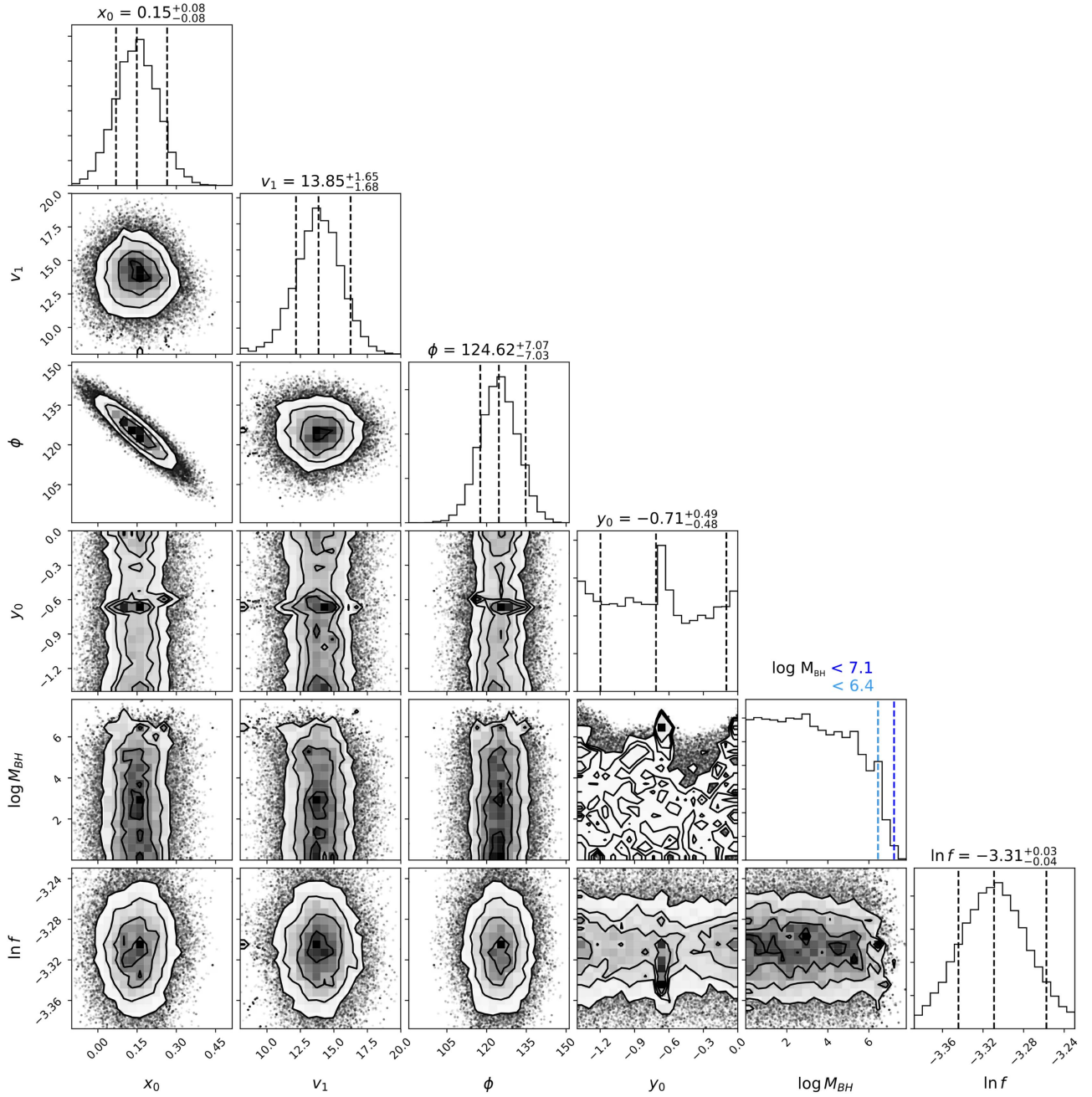


Figure 8. MCMC distributions for the velocity model fit to our data. Scatter plots are the projected two-dimensional distributions of the posterior probabilities of the parameters. Histograms display the one-dimensional distributions with vertical dashed lines drawn at the 16th, 50th, and 84th percentiles. The $\log M_{\text{BH}}$ histogram instead plots dark and light blue lines at the 99.7th (3σ) and 95.5th (2σ) percentiles respectively. From top-to-bottom and left-to-right, the panels display: x_0 (the position in degrees of the “central” velocity line at 261 km s^{-1}), v_1 (the linear component of velocity model in km s^{-1} per degree), ϕ (the angle that the normal to the x_0 axis makes with the horizontal), y_0 (the position of the black hole), $\log M_{\text{BH}}$ (the logarithm of the mass of the black hole in solar masses), and $\ln f$ (the natural logarithm of the fractional amount the errors are underestimated.)

$v_1 = 13.85_{-1.68}^{+1.65} \text{ km s}^{-1}$ per degree, $\phi = 124.62_{-7.03}^{+7.07}$ degrees, $y_0 = -0.71_{-0.48}^{+0.49}$ degrees, and $\ln f = -3.31_{-0.04}^{+0.03}$, with 1σ confidence. The significantly small value of $\ln f$ is an indication that our errors (v_{err}) are not underestimated. Plotted in the histogram for $\log M_{\text{BH}}$ in Figure 8 are 99.7th (3σ) and 95.5th (2σ) percentiles, indicating the upper limits on the mass for any BH within the central degree of the LMC to be $10^{7.1} M_{\odot}$ and $10^{6.4} M_{\odot}$ respectively. We found the observable signature of BHs of masses around $10^7 M_{\odot}$ to be slightly stronger than the natural fluctuation noise within our map. Our models containing a BH of a mass in the range of $10^{5-6} M_{\odot}$ fit the data with 1σ

confidence at a spatial position of $y_0 = -0^{\circ}.65$. This is plotted as an open circle on the data in Figure 6. However, considering that the detection has low statistical significance, and that the signatures of these sizes of BHs closely resemble the fluctuations in our data, we do not interpret this fit to indicate the presence of a BH.

In a separate analysis to the MCMC fit, we also constrained the presence of a BH through a χ^2 minimization. By first fitting a 2D plane described by Equation (3), we fit for the parameters x_0 , v_1 , and ϕ simultaneously. Then holding these three constant at their best-fit values, we performed the χ^2 minimization using

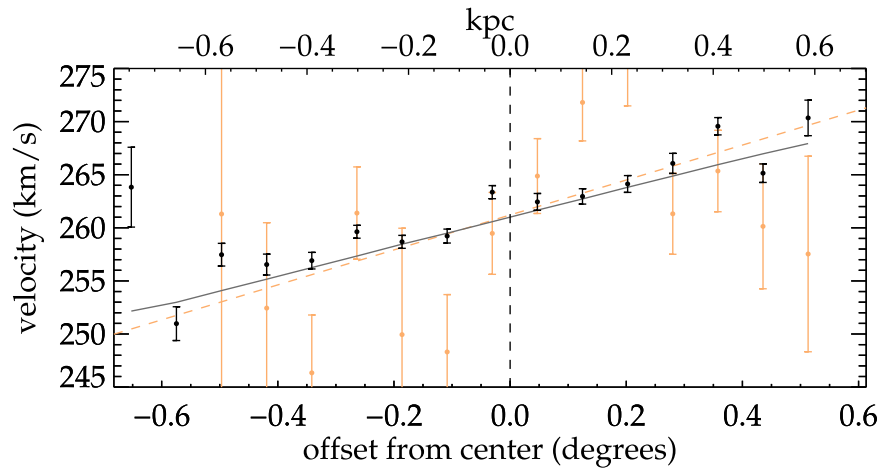


Figure 9. One-dimensional rotation curve for the LMC averaged over the entire field. Each black data point was found by taking a weighted mean of the velocity values from the 2D map in bins along the central line fit. Overplotted in orange are the binned LOS velocities for 256 individual stars compiled from the literature in van der Marel & Kallivayalil (2014) in our square degree field of view. The dashed line shows the best linear fit to these data.

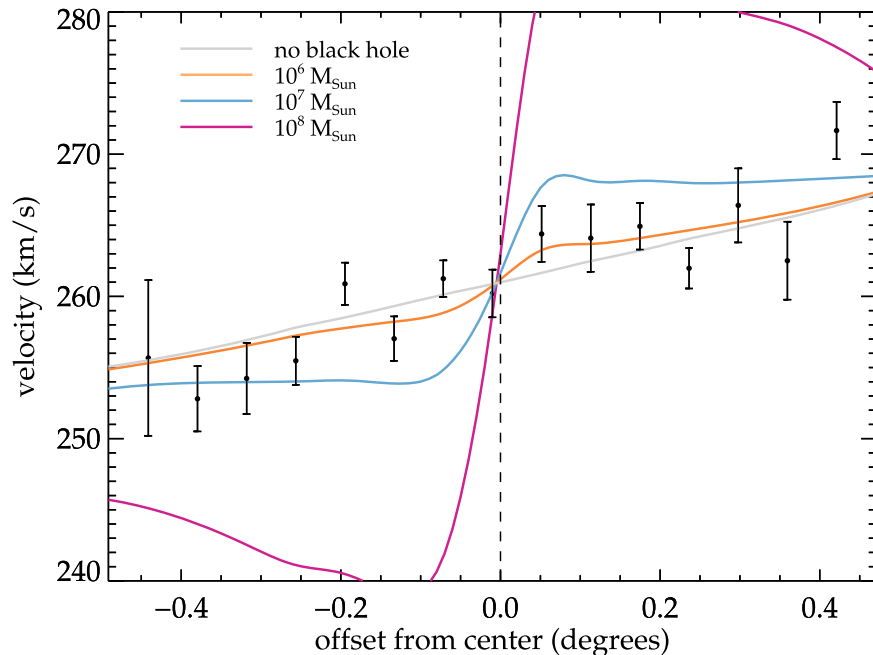


Figure 10. One-dimensional rotation curve for the LMC at the average position of the known kinematic center. Overplotted are the model rotation curves for fields with black holes of masses $10^6 M_{\odot}$, $10^7 M_{\odot}$, and $10^8 M_{\odot}$ at this location. Each data point in the one-dimensional curve was found by taking a weighted mean of velocity values from the 2D map within a 0.3° slice of the kinematic center.

Equation (1) as our model, varying both the position (y_0) and mass (M_{BH}) of the BH. The results yielded values consistent with the MCMC analysis. Most notably, the limit on the mass of the BH did not change.

3.4. One-dimensional Rotation Curve

The one-dimensional rotation curve of the data was produced by collapsing the velocity map along the axis perpendicular to the “central” line fit to the two-dimensional plane. This is displayed in Figure 9. Alternatively, Figure 10 displays the rotation curve in the region of the kinematic center with the rotation curves for BHs of varying masses overplotted. We performed a χ^2 -fit on this rotation curve of our data with the rotation curves of BH models, which yielded results consistent with the 2D fit.

Considering the entire central degree, the best known LOS model of this area comes from analysis done by van der Marel & Kallivayalil (2014) using global LOS velocities from various sources in the literature combined with large-scale *HST* proper motions in the LMC. Binning LOS data from the 256 individual stars in the study within our coverage area (displayed as the orange points in Figure 9) results in a slope of the rotation curve of $15.3 \pm 5.8 \text{ km s}^{-1}$ per degree. This is consistent with the slope of $13.9 \pm 1.6 \text{ km s}^{-1}$ per degree measured from our MUSE data and illustrates the significant improvement that our measurement for the rotation curve has over the previous data available.

4. Discussion and Conclusions

The center of the LMC is an enticing place to look for a central BH. If it hosts a BH, the proximity to our own galaxy

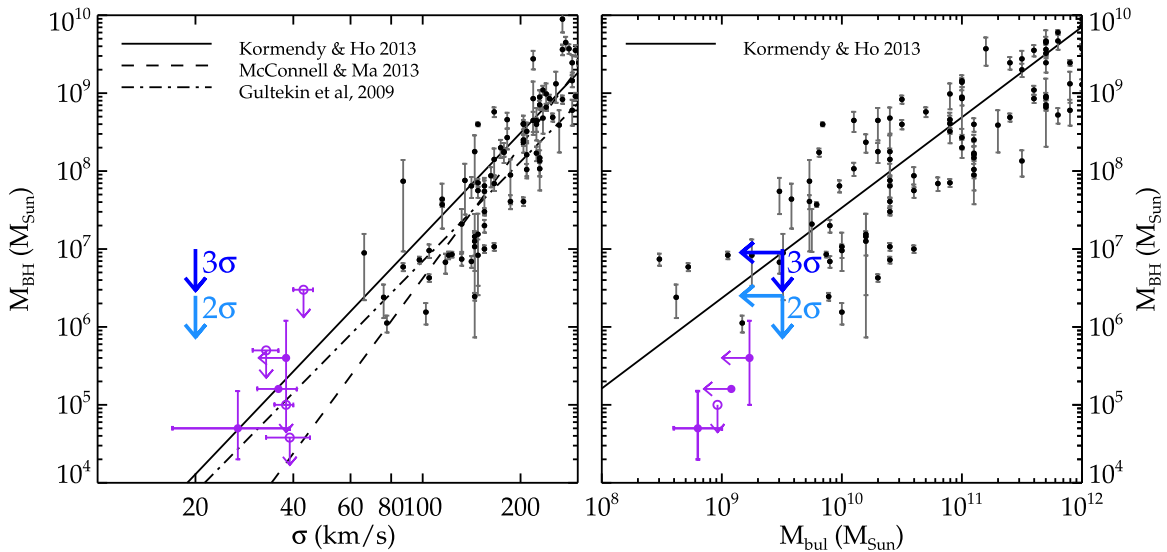


Figure 11. $M_{\text{BH}}-\sigma$ (left) and the $M_{\text{BH}}-M_{\text{bul}}$ (right) correlation for galaxies hosting supermassive black holes. Black data points are detections of BHs that come from the recent survey and compilation (Saglia et al. 2016). Black solid and dashed lines represent various determinations of the scaling relations in other works (Gültekin et al. 2009; Kormendy & Ho 2013; McConnell & Ma 2013). Our 3σ and 2σ upper limits for the BH mass in the LMC are indicated by the blue arrows. For the LMC, we use the disk velocity dispersion of $\sigma_{\text{disk}} \sim 20 \text{ km s}^{-1}$ (van der Marel & Kallivayalil 2014) and use the total baryonic mass of the LMC as an upper limit at $M_{\text{gal}} \sim 3.2 \times 10^9 M_{\odot}$ (van der Marel et al. 2002) since the LMC is a disk galaxy without a classical bulge (so $M_{\text{bul}} \ll M_{\text{gal}}$). Also plotted in filled purple circles are detections of black holes at the low-mass end: the smallest BH ever reported in a galactic nucleus RGG 118 (Baldassare et al. 2015), the well studied dwarf system POX 52 (Barth et al. 2004; Thornton et al. 2008), and the small and bulgeless galaxy NGC 4395 (Filippenko & Ho 2003; Peterson et al. 2005; den Brok et al. 2015). Open circles are upper-mass limits for BHs in low- σ galaxies: NGC 404 (Seth et al. 2010), IC 342 (Böker et al. 1999), NGC 205 (Valluri et al. 2005), and NGC 3621 (Barth et al. 2009).

would mean that this dwarf-galaxy/low-mass BH system is readily available to study in extreme detail. This could be a very significant test of the $M_{\text{BH}}-\sigma$ relation between BHs and their host galaxies at the lower-mass end and would contribute to constraining models of SMBH growth early in the universe (Greene 2012).

We have presented here the most detailed velocity field measurement for the center of the LMC to date, based on measurements with VLT/MUSE. We have used these new data to constrain the possible presence of a central BH in the LMC. We arrive at a 3σ upper-mass limit of $10^{7.1} M_{\odot}$ for a BH at the center of the LMC, or a 2σ upper limit of $10^{6.4} M_{\odot}$. We also report the slope of the rotation curve over the central region of the LMC to be measured with an improved precision of $13.9 \pm 1.6 \text{ km s}^{-1}$ per degree (or $15.8 \pm 1.8 \text{ km s}^{-1}$ per kpc). We found this measurement to be in agreement with the slope derived from binned measurements of LOS velocities from individual stars in the literature, but with a factor of four smaller uncertainty.

Shown in Figure 11 are two of the scaling relations observed between SMBHs and their host systems. The left panel describes the relationship between BH mass and the velocity dispersion of its host system, while the right describes the relationship between the BH mass and its host system’s bulge mass. Extrapolating these relations to a lower-mass range leads to the consideration of dwarf galaxies, nuclear clusters, and GCs with IMBHs of masses $< 10^6 M_{\odot}$. Our upper limit for the mass of a BH in the LMC is plotted in blue at both 2σ and 3σ confidence. They are plotted against estimates for the disk velocity dispersion ($\sigma_{\text{disk}} \sim 20 \text{ km s}^{-1}$ van der Marel & Kallivayalil 2014) and the total baryonic mass of the LMC ($M_{\text{gal}} \sim 3.2 \times 10^9 M_{\odot}$ van der Marel et al. 2002). It should be noted though that the known BH scaling relations for other

galaxies pertain to galaxy bulges. The LMC is a late-type Magellanic irregular disk galaxy. It does not have a well-defined bulge, and hence $M_{\text{bul}} \ll M_{\text{gal}}$. Moreover, while σ_{disk} for the LMC is well-measured, it is not clear whether it is meaningful to interpret it in the same way as for galaxy bulges. One alternative is to use the quadratic sum of the disk velocity dispersion and the rotational velocity of the LMC: $\sigma = \sqrt{\sigma_{\text{disk}}^2 + v_{\text{rot}}^2} \sim 93 \text{ km s}^{-1}$, where $v_{\text{rot}} = 91.7 \pm 18.8 \text{ km s}^{-1}$ (van der Marel & Kallivayalil 2014). This would shift our upper limits to the right on the $M_{\text{BH}}-\sigma$ relation. With these caveats in mind, our results are not inconsistent with any of the known scaling relations.

Also shown in Figure 11 are three notable measurements of IMBHs found in other dwarf galaxies in the last 15 years: POX 52 (Barth et al. 2004; Thornton et al. 2008), NGC 4395 (Filippenko & Ho 2003; Peterson et al. 2005; den Brok et al. 2015), and RGG 118 (Baldassare et al. 2015). Upper limits from other dynamical methods are also plotted for the nearby S0 type galaxy NGC 404 (Seth et al. 2010), the nuclear star cluster of spiral galaxy IC 342 (Böker et al. 1999), the dwarf elliptical galaxy NGC 205 (Valluri et al. 2005), and the bulgeless spiral galaxy NGC 3621 (Barth et al. 2009). Due to the difficulty in detecting BHs in this mass range, and the distance to these objects limiting our ability to measure detailed kinematics measurements in this regime remain scarce.

The limit we place on a BH in the LMC is unique in mapping individual stellar motions within the central 0.5 kpc of the host galaxy. This is the first measured upper-mass limit for a central BH in the LMC and by far the nearest dwarf galaxy with a kinematic limit on a central BH mass. The limit reinforces the expectation that if the LMC harbors any massive BH, it is in the intermediate-mass range. This new result is also of interest in the context of the detection of candidate




hypervelocity stars in/from the LMC (e.g., Bonanos et al. 2008; Przybilla et al. 2008; Boubert & Evans 2016; Lennon et al. 2017), which could be connected to the possible presence of a central BH.

This study is a promising step in understanding the complex dynamics of the LMC's central bar region. Performing a similar analysis of the central region over a smaller area with higher resolution and longer integration time could easily constrain this upper limit further. Or, if the LMC does harbor an IMBH, velocity maps generated from integral field spectrographs such as MUSE could very well detect its kinematic signature. Additionally, using our spectra to identify distinct stellar populations and generate velocity maps of these different populations would provide further insight into the complex dynamics and history of the LMC's bar.

Since the relations between BH mass and their host systems hold for galaxies with a wide range of properties, the growth of a central BH seems to be closely linked with the process of galaxy formation. The study of IMBHs in dwarf galaxies is therefore crucial for understanding BH growth and interaction with its surrounding host system. It is still unknown what fraction of low-mass galaxies contain BHs, and the measurements remain difficult to achieve. By studying one of the closest low-mass galaxies, the LMC, we can get a relatively close up view of a dwarf galaxy and determine the effects that any BH has on its components and structure. Further kinematic study could unveil any BH lurking within our complicated neighbor, especially if the position of its kinematic center can be pinned down more accurately.

This work was supported in part by the Leiden/ESA Astrophysics Program for Summer Students (LEAPS) and the Space Telescope Science Institute's (STScI) Space Astronomy Summer Program. Based on observations collected at the European Organisation for Astronomical Research in the Southern Hemisphere, Chile under ESO program 094.B-0566. This publication makes use of data products from the Two Micron All Sky Survey, which is a joint project of the University of Massachusetts and the Infrared Processing and Analysis Center/California Institute of Technology, funded by the National Aeronautics and Space Administration and the National Science Foundation. We would like to thank the anonymous referee for helpful comments and suggestions.

ORCID iDs

H. Boyce  <https://orcid.org/0000-0002-6530-5783>
 R. P. van der Marel  <https://orcid.org/0000-0001-7827-7825>
 N. Neumayer  <https://orcid.org/0000-0002-6922-2598>

References

- Alcock, C., Allsman, R. A., Alves, D. R., et al. 2000, *ApJ*, 542, 281
- Anderson, J., & van der Marel, R. P. 2010, *ApJ*, 710, 1032
- Bacon, R., Accardo, M., Adjali, L., et al. 2010, *Proc. SPIE*, 7735, 773508
- Baldassare, V. F., Reines, A. E., Gallo, E., & Greene, J. E. 2015, *ApJL*, 809, L14
- Barth, A. J., Ho, L. C., Rutledge, R. E., & Sargent, W. L. W. 2004, *ApJ*, 607, 90
- Barth, A. J., Strigari, L. E., Bentz, M. C., Greene, J. E., & Ho, L. C. 2009, *ApJ*, 690, 1031
- Begelman, M. C., Volonteri, M., & Rees, M. J. 2006, *MNRAS*, 370, 289
- Bertin, E., & Arnouts, S. 1996, *A&AS*, 117, 393
- Besla, G., Kallivayalil, N., Hernquist, L., et al. 2012, *MNRAS*, 421, 2109
- Besla, G., Martínez-Delgado, D., van der Marel, R. P., et al. 2016, *ApJ*, 825, 20
- Böker, T., van der Marel, R. P., & Vacca, W. D. 1999, *AJ*, 118, 831
- Bonanos, A. Z., López-Morales, M., Hunter, I., & Ryans, R. S. I. 2008, *ApJL*, 675, L77
- Boubert, D., & Evans, N. W. 2016, *ApJL*, 825, L6
- Cappellari, M. 2017, *MNRAS*, 466, 798
- Cappellari, M., & Emsellem, E. 2004, *PASP*, 116, 138
- Cole, A. A., Tolstoy, E., Gallagher, J. S., III, & Smecker-Hane, T. A. 2005, *AJ*, 129, 1465
- de Vaucouleurs, G., & Freeman, K. C. 1972, *VA*, 14, 163
- den Brok, M., Seth, A. C., Barth, A. J., et al. 2015, *ApJ*, 809, 101
- Dickey, J. M., & Lockman, F. J. 1990, *ARA&A*, 28, 215
- Feldmeier, A., Lützgendorf, N., Neumayer, N., et al. 2013, *A&A*, 554, A63
- Ferrarese, L., & Merritt, D. 2000, *ApJL*, 539, L9
- Filippenko, A. V., & Ho, L. C. 2003, *ApJL*, 588, L13
- Foreman-Mackey, D., Hogg, D. W., Lang, D., & Goodman, J. 2013, *PASP*, 125, 306
- Freedman, W. L., Madore, B. F., Gibson, B. K., et al. 2001, *ApJ*, 553, 47
- Gebhardt, K., Bender, R., Bower, G., et al. 2000, *ApJL*, 539, L13
- Gebhardt, K., Lauer, T. R., Kormendy, J., et al. 2001, *AJ*, 122, 2469
- Goodman, J., & Weare, J. 2010, *Commun. Appl. Math. Comput. Sci.*, 5, 65
- Greene, J. E. 2012, *NatCo*, 3, 1304
- Greene, J. E., & Ho, L. C. 2007, *ApJ*, 656, 84
- Gültekin, K., Richstone, D. O., Gebhardt, K., et al. 2009, *ApJ*, 695, 1577
- Häring, N., & Rix, H.-W. 2004, *ApJL*, 604, L89
- Hatzidimitriou, D., Cannon, R. D., & Hawkins, M. R. S. 1993, *MNRAS*, 261, 873
- Kallivayalil, N., van der Marel, R. P., Besla, G., Anderson, J., & Alcock, C. 2013, *ApJ*, 764, 161
- Kim, S., Staveley-Smith, L., Dopita, M. A., et al. 1998, *ApJ*, 503, 674
- Kormendy, J., & Ho, L. C. 2013, *ARA&A*, 51, 511
- Lanzoni, B., Mucciarelli, A., Origlia, L., et al. 2013, *ApJ*, 769, 107
- Lennon, D. J., van der Marel, R. P., Ramos Lerate, M., O'Mullane, W., & Sahlmann, J. 2017, *A&A*, 603, A75
- Lodato, G., & Natarajan, P. 2006, *MNRAS*, 371, 1813
- Luks, T., & Rohlfs, K. 1992, *A&A*, 263, 41
- Lützgendorf, N., Kissler-Patig, M., Noyola, E., et al. 2011, *A&A*, 533, A36
- Maccarone, T. J., Fender, R. P., & Tzioumis, A. K. 2005, *Ap&SS*, 300, 239
- Madau, P., Haardt, F., & Dotti, M. 2014, *ApJL*, 784, L38
- Marconi, A., & Hunt, L. K. 2003, *ApJL*, 589, L21
- McConnell, N. J., & Ma, C.-P. 2013, *ApJ*, 764, 184
- McNamara, B. J., Harrison, T. E., Baumgardt, H., & Khalaj, P. 2012, *ApJ*, 745, 175
- Merritt, D., Ferrarese, L., & Joseph, C. L. 2001, *Sci*, 293, 1116
- Mortlock, D. J., Warren, S. J., Venemans, B. P., et al. 2011, *Natur*, 474, 616
- Neumayer, N., & Walcher, C. J. 2012, *AdAst*, 2012, 709038
- Nikolaev, S., & Weinberg, M. D. 2000, *ApJ*, 542, 804
- Noyola, E., Gebhardt, K., & Bergmann, M. 2008, *ApJ*, 676, 1008
- Olsen, K. A. G., & Salyk, C. 2002, arXiv:astro-ph/0207077
- Peterson, B. M., Bentz, M. C., Desroches, L.-B., et al. 2005, *ApJ*, 632, 799
- Przybilla, N., Fernanda Nieva, M., Heber, U., & Butler, K. 2008, *ApJL*, 684, L103
- Reines, A. E., Greene, J. E., & Geha, M. 2013, *ApJ*, 775, 116
- Reines, A. E., Sivakoff, G. R., Johnson, K. E., & Brogan, C. L. 2011, *Natur*, 470, 66
- Saglia, R. P., Opitsch, M., Erwin, P., et al. 2016, *ApJ*, 818, 47
- Schenck, A., Park, S., & Post, S. 2016, *AJ*, 151, 161
- Seth, A. C., Cappellari, M., Neumayer, N., et al. 2010, *ApJ*, 714, 713
- Skrutskie, M. F., Cutri, R. M., Stiening, R., et al. 2006, *AJ*, 131, 1163
- Strader, J., Chomiuk, L., Maccarone, T. J., et al. 2012, *ApJL*, 750, L27
- Thornton, C. E., Barth, A. J., Ho, L. C., Rutledge, R. E., & Greene, J. E. 2008, *ApJ*, 686, 892
- Valluri, M., Ferrarese, L., Merritt, D., & Joseph, C. L. 2005, *ApJ*, 628, 137
- van der Marel, R. P. 2001, *AJ*, 122, 1827
- van der Marel, R. P., Alves, D. R., Hardy, E., & Suntzeff, N. B. 2002, *AJ*, 124, 2639
- van der Marel, R. P., & Kallivayalil, N. 2014, *ApJ*, 781, 121
- Van der Swaelmen, M., Hill, V., Primas, F., & Cole, A. A. 2013, *A&A*, 560, A44
- Volonteri, M., & Natarajan, P. 2009, *MNRAS*, 400, 1911
- Walker, A. R. 2012, *ApSS*, 341, 43
- Zhao, H., & Evans, N. W. 2000, *ApJL*, 545, L35